A Smart Nanoassembly for Multistage Targeted Drug Delivery and Magnetic Resonance Imaging

Zhenhua Li, Kai Dong, Sa Huang, Enguo Ju, Zhen Liu, Meili Yin, Jinsong Ren, and Xiaogang Qu**

Efficient delivery of DNA-toxin anticancer drugs into nucleus of targeted tumor cells while simultaneously minimizing the side effects to normal tissue is a major challenge for cancer therapy. Herein, a multistage continuous targeting strategy based on magnetic mesoporous silica nanoparticles to overcome the challenge is demonstrated. At the initial-stage, the magnetic nanoparticle is capable of efficiently accumulating in tumor tissue guided by magnet. Following by the magnetic targeting, the targeting ligand gets it right into the cancer cell by receptor-mediated endocytosis. Accompanied by endocytosis into the lysosomes, the nanoparticle reverses its surface charge from negative to positive which leads to the separation of charge-conversional polymer from the nanoparticle to re-expose the nuclear-targeting TAT peptide. Finally, TAT peptide facilitates the carriers to enter nucleus and the DNA-toxin camptothecin can inhibit topoisomerase I to induce cell apoptosis. Furthermore, the nano-drug delivery system can be simultaneously used as predominant contrast agents for magnetic resonance imaging. This proof of concept might open the door to a new generation of carrier materials in the fields of targeted drug transport platform for cancer theranostics.

1. Introduction

Recently, nanoparticle-based drug delivery is receiving increasing attention for cancer treatments due to their improved pharmacokinetics and biodistribution profiles via the enhanced permeability and retention (EPR) effect.[1] However, the EPR effect can only enhance the accumulation of nanocarriers in tumor tissues; the poor cellular internalization limits the utilization of anticancer drugs, which hampers the efficacy of cancer chemotherapy.[2] One approach to overcoming these limitations is to attach membrane receptor-targeting moieties to the nanoparticle surfaces.[3] Nanoparticles that present targeting moieties can bind to target cells through ligand-receptor interactions that induce receptor-mediated endocytosis.[4] This delivery strategy achieves a high targeting specificity and delivery efficiency, while avoiding nonspecific binding. However, the cellular uptake and internalization of these functionalized nanocarriers along with the loaded cargo occurs by a receptor-mediated endocytosis pathway, leading to the problem that some compounds are trapped in endosomes or lysosomes and cannot reach the biological targets in the cytoplasm or nucleus.[5] In addition, drug-resistant cancer cells have many intracellular drug-resistance mechanisms to limit the access of cytosolic drugs to the targeted organelle.[6] Thus, to elicit their pharmacological responses, how these carriers can localize at the biological targets is a key step. Different organelle localization signal molecules have been used for the decoration of nanoparticles surface to overcome this challenge.[7] For example, Torchilin and co-workers designed a paclitaxel loaded and triphenylphosphonium-PEG-PE conjugated liposomes to achieve mitochondria targeted cancer therapy;[8] Shi and co-workers employed TAT peptide conjugated mesoporous silica nanoparticles (MSNs-TAT) for nuclear-targeted drug delivery.[9] Although organelle-targeting moieties have favourable features, the triphenylphosphonium (TPP) and TAT peptide are highly positively charged at physiological pH and the nanoparticles can cause severe serum inhibition and can be rapidly cleared from the plasma compartment.[10] Furthermore, these single targeting group based nanoparticles could not discern between diseased cells and healthy cells, leading to systemic toxicity with undesired side effects.[11] Therefore, nanoparticle functionalized with individual targeting groups, such as tumor tissue-targeting elements, membrane receptor-targeting molecules or organelle-targeting moieties, is not an optimal option for drug delivery. An easy-to-fabricate nanoassembly that can achieve successive targeting process from tumor tissue to organelles for anticancer drug delivery is still lacking and remains highly desirable.

Z. Li, K. Dong, E. Ju, Z. Liu, M. Yin, Prof. J. Ren, Prof. X. Qu
State Key Laboratory of Rare Earth Resources Utilization and Laboratory of Chemical Biology
Changchun Institute of Applied Chemistry
Chinese Academy of Sciences
Changchun 130022, China
E-mail: jren@ciac.ac.cn; xqu@ciac.ac.cn
Z. Li, K. Dong, E. Ju
University of Chinese Academy of Sciences
Beijing 100039, China
Dr. S. Huang
Department of Radiology
The Second Hospital of Jilin University
Changchun, Jilin 130041, China

DOI: 10.1002/adfm.201303662

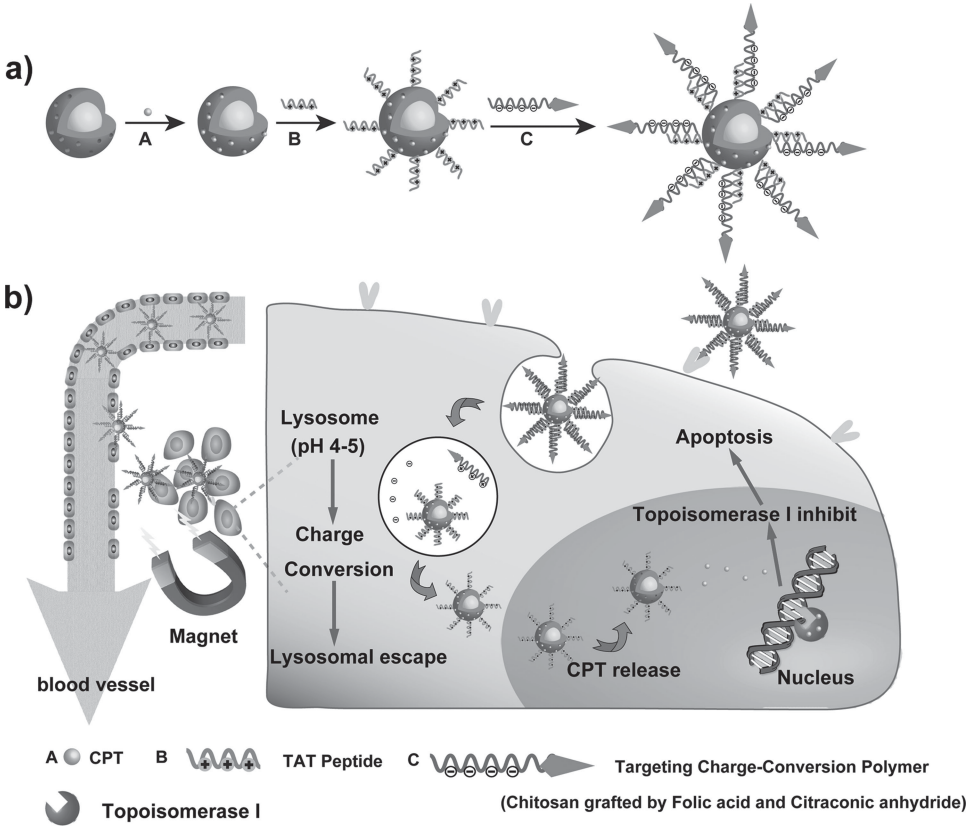

Figure 1. Structure of FMSN@CPT-TAT/FA-CS-Cit and multistage continuous targeting drug delivery process. a) Functionalization protocol of FMSN and drug loading. b) The cascade nuclear drug delivery. Nanovector was accumulated in tumor via magnetic targeting and then internalized by folic acid-receptor mediated endocytosis. Subsequently, charge-conversion was triggered by lysosome and regenerated the positively charged TAT for nuclear-targeted nanodrug delivery.

In this work, for the first time, we demonstrate a multistage continuous targeting strategy based on magnetic mesoporous silica nanoparticles (FMSN) for nuclear drug delivery (**Figure 1**). The Fe_3O_4 nanocore of the FMSN has multiple functionalities applicable to simultaneous magnetic resonance imaging and magnetic targeting to direct drugs to localized sites.[12] In addition, there are some unique properties after coating by mesoporous silica, such as high drug loading capability resulting from their high specific surface area, large pore volume, and easy surface modification.[13] Meanwhile, cell-penetrating peptide derived from the human immunodeficiency virus 1 (HIV) transactivator protein (TAT) was conjugated to FMSN for the enhancement of nuclear-targeting efficiency. The nanoparticle was further decorated with charge-conversional polymer to temporarily shield the positive charge of TAT peptide which could enhance stability of nanoparticles in physiological conditions and prolong circulation time in blood. Citraconic anhydride (Cit) and folate-grafted chitosan (designated as FA-CS-Cit) was used as the charge-conversional polymer. Citraconic anhydride is α-methyl derivative of maleic anhydride and it is easy to react with chitosan to form amide. The citraconic amide is stable at both neutral and basic pH, but it becomes unstable at acidic endo-/lysosomal (pH 4–5) conditions and promptly degrades back into the cationic primary amine.[14] The negative-to-positive charge-conversional chitosan was also functionalized with folic acid (FA) moieties for targeting tumor cells that overexpressed folate receptors. Thus, in this smart drugs delivery system, multistage continuous targeting strategy was ingeniously designed to enhance the efficacy of cancer chemotherapy and minimize the side effects to normal tissue. Typically, at the initial-stage, nanoparticles would efficiently accumulate in target tissues guided by local strong magnetic field generated by a magnet. Accompanied by the accumulation of nanocarriers in target tissues, the subsequent-stage of cancer cell targeting process took place in which the accumulated nano-drug carriers would be efficiently internalized by cancer cells via a folate-receptor-mediated endocytosis mechanism. Once the nanovectors arrived at the acidic lysosomes, the citraconic amides of charge-conversional chitosan were quickly hydrolyzed, regenerated chitosan, detached from nanoparticle, and then re-exposed the final-stage of the nuclear-targeted TAT peptide groups. Since chitosan was able to rupture lysosomes via the ''proton-sponge'' effect, the regenerated chitosan could help the nanoparticles to escape from the lysosomes into the cytosol.[15] The reactivated TAT peptide on the outside surface of FMSN could be recognized by the nuclear pore complexes (NPCs) and thus could guide the nanoparticles to transport from the cytosol into cell nuclei.[16] Aided by these three-stage continuous targeting process, the DNA-toxin camptothecin (CPT) successfully entered the nuclei of cancer cells to induce

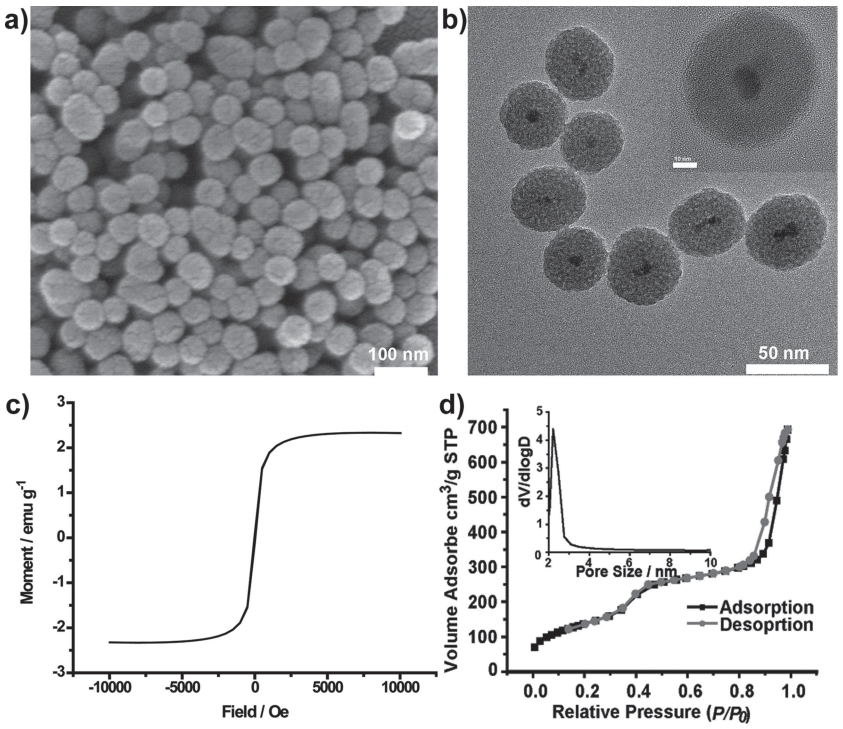

Figure 2. a) SEM and b) TEM images of core-shell FMSNs. c) Field-dependent magnetization at 300 K. d). N_2 adsorption/desorption isotherms (inset: pore size distribution from adsorption branch). The inset b) shows the high magnification image.

cell apoptosis. Furthermore, owing to the strong magnetic property of FMSN nanoparticles, the nanocarriers could be simultaneously used as predominant contrast agents for magnetic resonance imaging.

2. Results and Discussion

The mesoporous silica-encapsulated Fe_3O_4 nanocrystals (FMSN) were prepared according to the modified method reported previously.[17] As shown in **Figure 2**a, the FMSN was composed of monodisperse and uniform sphere-like nanoparticles and the average diameter was approximately 50 nm. Transmission electron microscopy (TEM) showed that 10 nm Fe_3O_4 core located at the center of $mSiO_2$ sphere, indicating the successful formation of FMSN nanoparticles (Figure 2b). The Fe concentration of FMSN was 25.225 μg/mg and the weight ratio of Fe_3O_4 to the total FMSN was 3.48%. The wormhole-like mesopores with diameters of around 2–3 nm were observed in the silica shells. The Fe_3O_4 core had multiple functionalities which was applicable to simultaneous magnetic targeting and magnetic resonance imaging. Field-dependent magnetism of FMSN particles at 300 K showed no hysteresis (Figure 2c), demonstrating that they were superparamagnetic. N_2 adsorption–desorption isotherms and BJH pore-size distribution curves gave a typical type IV curve with a specific surface area of 485 m^2g^{-1}, an average pore diameter of 2.5 nm and a narrow pore distribution, which were consistent with the TEM results (Figure 2d). For fluorescence imaging, fluorescein isothiocyanate (FITC) was incorporated covalently into the silica walls by treating FITC with 3-aminopropyltrieth-oxysilane and carrying out a subsequent silica sol-gel reaction. The dye-derivatized nanoparticles (FMSN@FITC) dispersed in water showed the typical emissions of fluorescein at 516 nm (Figure S1, Supporting Information). Following this, the synthesis of multistage continuous targeting nanocarriers was carried out in a two-step procedure. The conjugation of TAT peptide on the outside surface of the FMSN by an esterification reaction was confirmed by Fourier-transform infrared (FTIR) spectroscopy. As shown in Figure S2b (Supporting Information), the appearance of 1562 cm^{-1}, 1460 cm^{-1}, and 2975–2845 cm^{-1} corresponded to the acylamide vibration and C–H stretching vibration, respectively. Another peak can be observed at 1190 cm^{-1} due to C–N stretching mode of the amine groups on TAT peptide. These features demonstrated the surface embarking of TAT peptide. The folic acid attached FMSN (FMSN-FA) was also synthesized as a control nanocarrier. The successful grafting of FA onto the amine-functionalized FMSN was validated by FTIR spectroscopy. After surface functionalization with folate, a new peak assigned to CONH groups can be observed at 1652 cm^{-1} for the FMSN-FA. Moreover, the appearance of new peak at 1606 cm^{-1} and 1700 cm^{-1}, which were a typical vibration of folate (Figure S2a, Supporting Information), also proved successful conjugation of FA with FMSN.

To shield the cationic charges of TAT and simultaneously achieve cascade nuclear-targeting drug delivery, a negative-to-positive charge-reversal polymer triggered by the lysosomal pH was designed (Figure S3, Supporting Information). Chitosan (CS), which has abundant functional amino groups on the backbone for grafting citraconic anhydride, has attracted increasing attention in drug delivery systems due to its excellent properties such as biocompatibility, biodegradability, non-toxicity, immunogenicity, and bioadhesivity.[18] Folic acid (FA) moieties were first reacted with chitosan for folate-receptor targeting. For the preparation of FA-CS conjugates, EDC and NHS were used to activate the γ-COOH group of folate and formed an active intermediate. This intermediate was then reacted with the amine group of CS to form FA-CS by a stable amide bond. The FTIR spectra of CS and FA-CS were presented in Figure S4, Supporting Information. Significant differences could be observed when comparing the FTIR spectrum of FA-CS with that of CS. The absorption peaks at 1646 and 1514 cm^{-1} were weakened because of the substitution of folate with amine groups. In addition, the appearance of a new peak at 1606 cm^{-1}, which was a typical vibration of folate, confirmed the successful conjugation of chitosan with folate. The structure of grafting FA was also indicated by ^{1}H-NMR spectroscopy as shown in Figure S5, Supporting Information. Compared with the ^{1}H-NMR spectrum of CS, new signals appeared in the spectrum of FA-CS due to the introduction of folate (Figure S5b, Supporting Information). The peaks at 8.65, 7.69, and 2.53 ppm

were characteristic signals of the pteridine ring, benzene ring and methylene of folate. The FA-CS was then reacted with citraconic anhydride (Cit) to convert the primary amines into amides. The resulting amides had negative charges owing to the carboxylate groups at the end. The absorption value ratios between characteristic bands of 500–1000 cm^{-1} were attributed to the conjugation of chitosan with Cit (Figure S4, Supporting Information). Furthermore, ^{13}C-NMR spectra (in D_2O) of the FA-CS-Cit were also presented in Figure S6a,b, Supporting Information. Compared with FA-CS, the appearance of a new peak at 178.68 and 173.9 ppm corresponded to the carbon atom of C=O group in Cit units. The peaks centered at 151.98 and 127.13 ppm could be attributed to the two carbon atoms of the C=C–C. The grafting ratio of folic acid and citraconic anhydride to monosaccharide residue of CS was about 16.7% and 47.7% (Figure S6c, Supporting Information). The FTIR and ^{13}C-NMR spectrum together proved the presence of Cit. Finally, CS-FA-Cit was incubated with FMSN-TAT in PBS buffer to form FMSN-TAT/FA-CS-Cit complex through electrostatic interaction for the purposes of masking cationic charges of TAT peptide. TEM (Figure S7, Supporting Information) showed that the FMSN-TAT/FA-CS-Cit nanoparticles retained the pore structure and a layer of soft materials surrounded the FMSN. The successful deposition of FA-CS-Cit was also indicated by the change of zeta potential value and hydrodynamic diameters (Figure S8, Supporting Information). Since assessment of the safety for a nanovector was important for further application in vitro and in vivo, the cellular toxicities of as-prepared simples were first evaluated by a conventional MTT assay. The viability of HeLa and A549 cells was measured in the presence of nanoparticles at various concentrations (50–800 μg mL^{-1}). All of the nanoparticles showed low cytotoxicity even at concentrations up to 800 μg mL^{-1} (Figure S9, Supporting Information). These results indicated that FMSN-TAT/FA-CS-Cit exhibited no apparent cytotoxicity to cells and were favorably biocompatible.

The charge-conversional behaviour of the FA-CS-Cit polymer was monitored on the basis of the change in zeta potential after incubation at pH 7.4 and 5.6 (Figure S10, Supporting Information). The FMSN-TAT/FA-CS-Cit revealed a zeta potential of about –24 mV at pH 7.4 even after more than 18 h, indicating that they were always negatively charged as a result of the presence of COOH groups and the polymer was stable at physiological pH and capable of shielding the cationic charges of TAT peptide. However, at pH 5.6, the zeta potential gradually reached about +22 mV in about 8 h owing to the fact that citraconic amides were quickly hydrolyzed and exposed the positive charges of TAT groups. The key process for achieving nuclear drug delivery was that the nanoparticles should localize in acidic endosome/lysosomes to reactivate the nuclear-targeting TAT groups and subsequently escape from the lysosome and traverse to the nucleus. To observe the subcellular distribution, nanoparticles were first tagged by FITC and then a subcellular compartment labeling method was carried out using fluorescence microscopy imaging (**Figure 3**). Overlaying the images taken from FITC (green) and LysoTracker channels (red) yielded many yellow spots, suggesting that most FMSN@FITC-TAT/FA-CS-Cit was in the lysosomes. Importantly, the green spots in the nuclear region indicated that some FMSN@FITC-TAT nanoparticles were successfully escape from the lysosomes and entered the nuclei (Figure 3f). This result was in good agreement with our hypothesis.

To confirm the multistage continuous targeting ability of the nanoassemblies, we first demonstrated that FMSN-TAT/FA-CS-Cit could be used as an efficient magnetic vector for delivering CPT into cells. HeLa cells were incubated with CPT-loaded FMSN-TAT/FA-CS-Cit (FMSN@CPT-TAT/FA-CS-Cit) at 37 °C in the presence of a magnetic field. After 24 h incubation, cells near the magnet were effective destructed, while those far from the magnet were essentially unaffected (**Figure 4**) which was confirmed by a LIVE (green)/DEAD (red) kit and MTT assay. These results clearly demonstrated the unique magnetic targeted cancer cell ability using our FMSN@CPT-TAT/FA-CS-Cit. Next, the nanoassemblies were demonstrated for cascade cancer cell nuclear targeting. HeLa cells (FA+) and A549 cells (FA-) were chosen as target cells and control cells, respectively.[19] The cellular uptake and intracellular trafficking of FITC-labeled nanoparticles were observed with fluorescent microscopy imaging (**Figure 5**a–d and Figure S11a–d, Supporting Information). It could be first seen from the figure that very few green nanoparticles were observed in the two types of cells and most of them located in the cytoplasm after incubation with FMSN@FITC. Next we incubated FA-functional FMSN@FITC complexes with cells to reveal the high efficiency of internalization of nanocarriers. As expected, a strong green fluorescence was truly observed in HeLa cells. In contrast, no distinct fluorescence was seen for A549 cells (FA-), implying the special interaction between FA

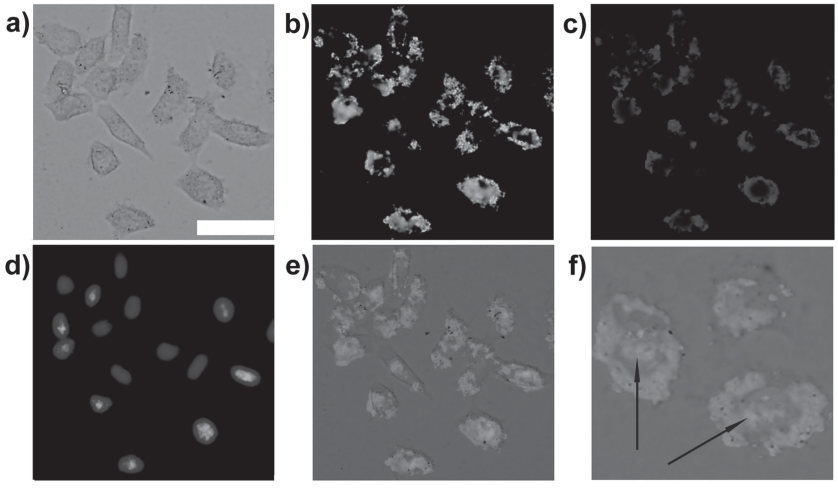

Figure 3. Localization of FMSN@FITC-TAT/FA-CS-Cit at endosomes/lysosomes in HeLa cells observed by florescence microscopy. a) brightfield, b) FITC, c) lysotracker, d) Hoechst 33258, and e,f) overlay. The arrow of enlarged image marked nuclear localization of nanoparticles. The scale bar is 50 μm.

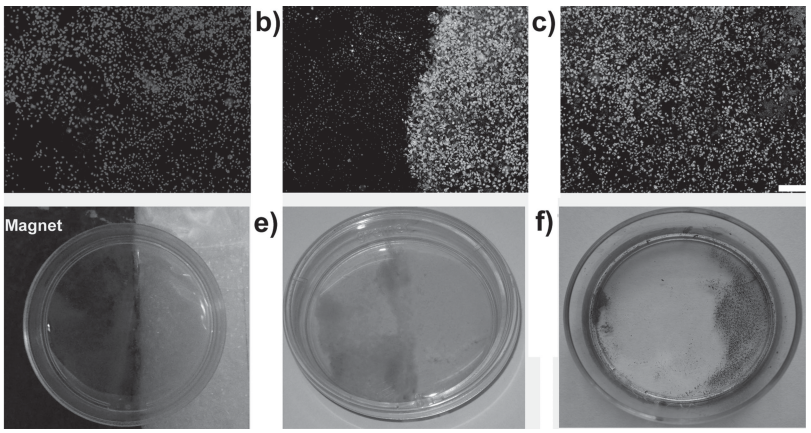

Figure 4. Magnetic guidance eliminated cancer cells. a–c) Fluorescence microscopy images of calcein AM (green, live cells) and propidium iodide (red, dead cells) co-stained cells after magnetic targeted drug delivery. Images were taken at different locations in the culture dish: a) close to the magnet, b) in the middle, and c) far from the magnet. d–f) Photographs represent the ability of magnetic targeting and cytotoxicity tested by MTT assay. d) A photo showing the experimental set-up: A magnet was placed close to the cell culture dish. e) A digital photo of the cell culture dish after magnetic targeted. f) After 24 h incubation, cell viability was tested by MTT assay. FMSN@CPT nanoparticles at 0.1 mg mL^{-1} were used in the above in vitro experiments. The scale bar is 200 μm.

and FA receptors overexpressed on HeLa cells. After having demonstrating the cascade magnetic and folate targeting ability of these multifunctional nanoparticles, we finally carried out the nuclear-targeting ability of TAT peptide attached particles. As expected, FMSN@FITC-TAT was mainly located in both the cytoplasm and the nuclei of the two types of cells. However, as mentioned above, the positively charged TAT peptide was easily cleared from the plasma compartment and cannot achieve the selective cell internalization. It was necessary to introduce the targeting and lysosome-triggered polymer for masking the positively charged TAT peptide temporarily. To achieve that, the intelligent FMSN@FITC-TAT/FA-CS-Cit nanoparticles were then incubated with HeLa and A549 cells, and we could clearly see that nanoparticles located in both the cytoplasm and the nuclei of HeLa cells, as demonstrated by the green fluorescence from the nuclei lighting up by FITC. However, negligible fluorescence was observed upon the incubation with A549 cells, which was further verified the FA receptor-mediated endocytosis mechanism of the particles. It indicated that the citraconic amides in FA-CS-Cit were hydrolyzed in the acidic lysosomes, detached from FMSN@FITC-TAT and finally regenerated the nuclear-targeting TAT in the acidic lysosomes, then FMSN@FITC-TAT nanoparticles successfully escaped from lysosomes and quickly entered the nuclei. The cellular uptake and nuclear targeting ability of FITC-labeled nanoparticles were also evident from flow cytometry experiments (Figure 5e) and the FACS analysis results were consistent with the fluorescence microscopy images. Taken together, these results supported our claims that FMSN-TAT/FA-CS-Cit was an ideal vector for nuclear-drug delivery.

Magnetic resonance imaging (MRI) is among the best non-invasive techniques used in clinical medicine for assessing anatomy and function of tissues. In addition, it offers several advantages such as excellent temporal and spatial resolution, no direct exposure to radioactive compounds and rapid in vivo acquisition of images.[20] The potential of using the FMSN@FITC-TAT/FA-CS-Cit for MRI imaging was then investigated. As expected, FMSN@FITC-TAT/FA-CS-Cit showed drastically reduced signals in T_2-weighted MR images (Figure 5f). In order to verify the feasibility of FMSN@FITC-TAT/FA-CS-Cit as high-performance MRI nanoprobe in vivo, nanoparticles were suspended in 0.9 wt% NaCl solution and administrated to H22 tumor-bearing mouse through intravenous injection. Then T_2-weighted MR imaging was conducted after the tail vein injection of FMSN@FITC-TAT/FA-CS-Cit. Figure 5g showed obvious darkening effects in the tumor after administration, demonstrating the feasibility of using these nanoparticles as MRI contrast agents in vivo.

CPT is a DNA-toxin drug that inhibits topoisomerase involved in DNA replication to induce cell death. The drug loading in nanoparticles was about 5.2 wt% as determined by UV-Vis spectroscopy (Figure S12a, Supporting Information). CPT is a hydrophobic anticancer drug and the release of CPT was negligible at aqueous solution (Figure S12b, Supporting Information). Cell apoptosis induced by various CPT-loaded nanovectors was compared using annexin V–fluorescein isothiocyanate (Annexin V-FITC) and propidium iodide (PI) staining assay (Figure S13a,b, Supporting Information). In the absence of cell penetrating peptides TAT, analogous (≈23%) cell apoptosis was induced treated by FMSN@CPT with two types of cells. Compared to FMSN@CPT, the FMSN@CPT-FA showed a higher staining for the apoptosis marker phosphatidylserine (PS) by Annexin-V with HeLa cells. In contrast, a lower staining was obtained from incubation with A549 cells which was attributed to the specific binding and uptake of the nanocarries to the target cancer cells mediated by folic acid. Next, the cell apoptosis induced by FMSN@CPT-TAT against HeLa and A549 cells were tested. After 24 h of incubation with FMSN@CPT-TAT, most of the cancer cells stained for both PI and Annexin-V suggesting late apoptotic phase (Q2). Importantly, no obvious apoptosis of A549 cells was induced when TAT peptide was masked by FA conjugated charge-conversional polymer while a much higher percentage of apoptotic HeLa cells after treatment with FMSN@CPT-TAT/FA-CS-Cit could be clearly observed. The substantially increased cell apoptosis was attributed to the fact that the CPT could effectively enter the nuclei of the targeting cells transported by the smart carrier. In addition, the cells remained viable in the presence of free CPT suspended in PBS, indicating that the drug was not internalized by the cells due to its poor solubility. Standard methyl thiazolyl tetrazolium (MTT) assay was also carried out to determine relative viabilities of cells at 24 h post various treatments. As shown in **Figure 6**a,b, exposure to our nanovectors resulted in a dose-dependent decrease in cell viability

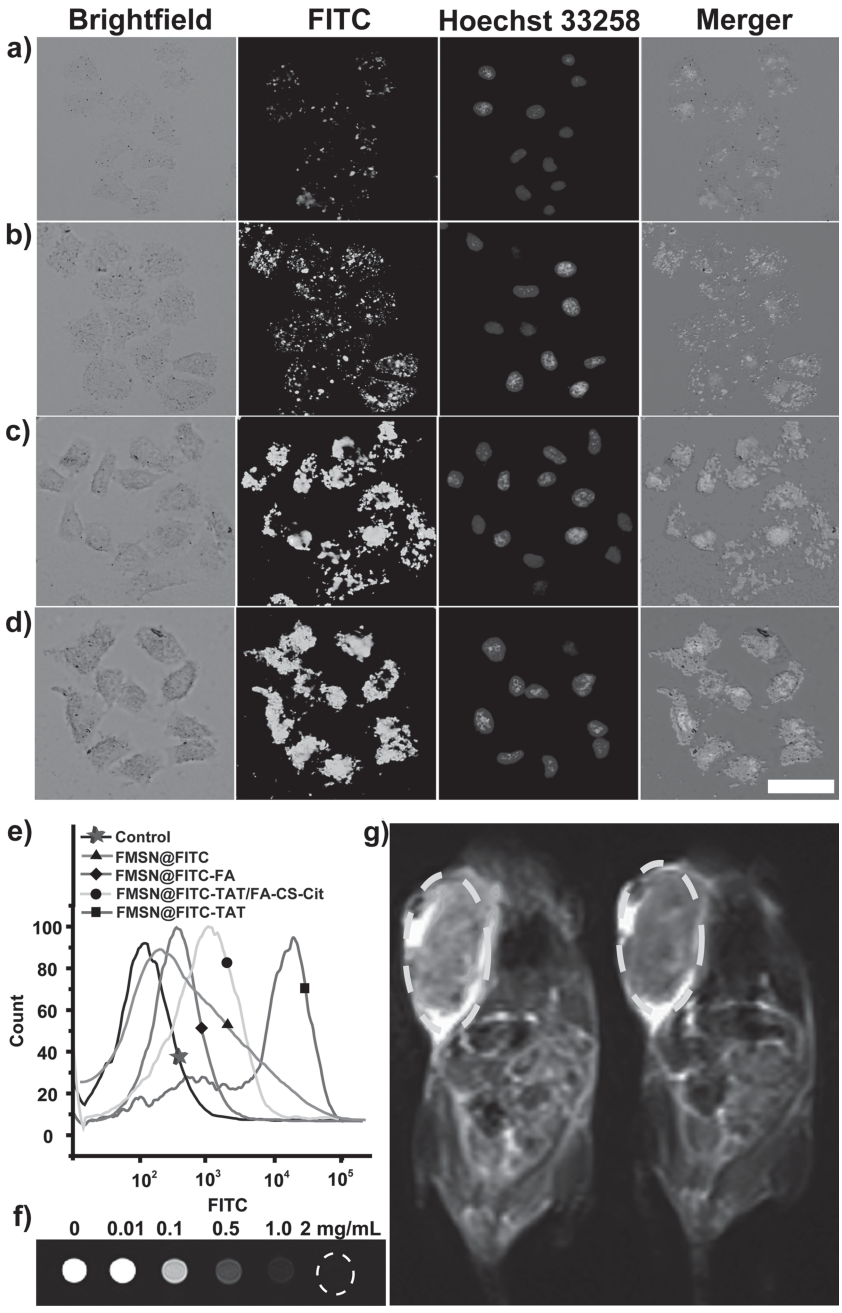

Figure 5. Fluorescence microscope images of HeLa cells incubated with FMSN@FITC a), FMSN@FITC-FA b), FMSN@FITC-TAT/FA-CS-Cit c), and FMSN@FITC-TAT d). Flow cytometry analysis e) of HeLa cells treated with FITC-labeled nanoparticles. f) Phantom NMR images of FMSN@FITC-TAT/FA-CS-Cit dissolved in PBS solution showing T_2-weighted contrast. g) T_2-weighted MR images of a H22 tumor-baring mouse before and after injection of FMSN@FITC-TAT/FA-CS-Cit nanoparticles through the tail vein. The scale bar is 20 μm.

and corresponding with FACS results, the FMSN@CPT-TAT/FA-CS-Cit showed a remarkably higher cytotoxic efficacy with targeting HeLa cells. Taking together, the enhanced toxicity of FMSN@CPT-TAT/FA-CS-Cit for target cells were clearly benefited from the multistage continuous targeting drug delivery system.

3. Conclusions

In summary, we designed and fabricated a novel type of intelligent nanovector for multistage continuous targeting drug delivery and imaging. The nuclear localizing nanocarriers successfully escorted DNA-toxin CPT directly to nucleus through accurate guidance and released drugs to induce cell apoptosis. The use of this smart system provided unprecedented advantages over other nanoparticle-based drug delivery systems. First, magnetic guidance was used to enhance the accumulation of nanovector in tumor which was superior to passive drug targeting systems. Second, targeting ligand was introduced into the nano-drug delivery system to enhance the cellular uptake and elucidate the regeneration of TAT peptide in endo/lysosomes. Third and importantly, the positive charges of nuclear-targeting TAT peptides were shielded by a negative-to-positive charge-reversal polymer to suppress their nonspecific interactions and then reactivated by lysosomal pH. Moreover, magnetic targeting, folate-targeted and nuclear targeting were not independent but pieced together into a cascade targeting process for nuclear-targeting. In vitro results indicated that FMSN@CPT-TAT/FA-CS-Cit achieved enhanced cell growth inhibition efficiency in cancerous cells. In addition, the FMSN@CPT-TAT/FA-CS-Cit system could be used as predominant contrast agents for magnetic resonance imaging. Collectively, these findings suggest that the novel multistage continuous targeting nanostructure should show great potential for cancer therapy.

4. Experimental Section

Chemicals and Materials: Nanopure water (18.2 Meghom·cm; Millpore Co., USA) was used in all experiments and to prepare all buffers. N-cetyltrimethylammonium bromide (CTAB), EDC, Sulfo-NHS aminopropyltriethoxysilane (APTES) were obtained from Alfa Aesar. Fuorescein isothiocyanate (FITC), tetraethylorthosilicate (TEOS), camptothecin (CPT), and citraconic anhydride were purchased from Sigma-Aldrich. Chitosan (molecular weight = 5495.1, number-average molecular weight and M_w/M_n = 2.299) was obtained from Golden-shell Biochemical Co., LTD. TAT (YGRKKRRQRRR) was purchased from China Peptides CO., LTD.

Measurements and Characterizations: A field emission scanning electron microscope (FESEM, S4800, Hitachi) equipped with an energy-dispersive X-ray (EDS) spectrum was applied to determine the morphology and composition of the as-prepared samples. TEM was performed on a JEOL 1011 transmission electron microscope at an accelerating voltage of 200 kV. N_2 adsorption-desorption isotherms were

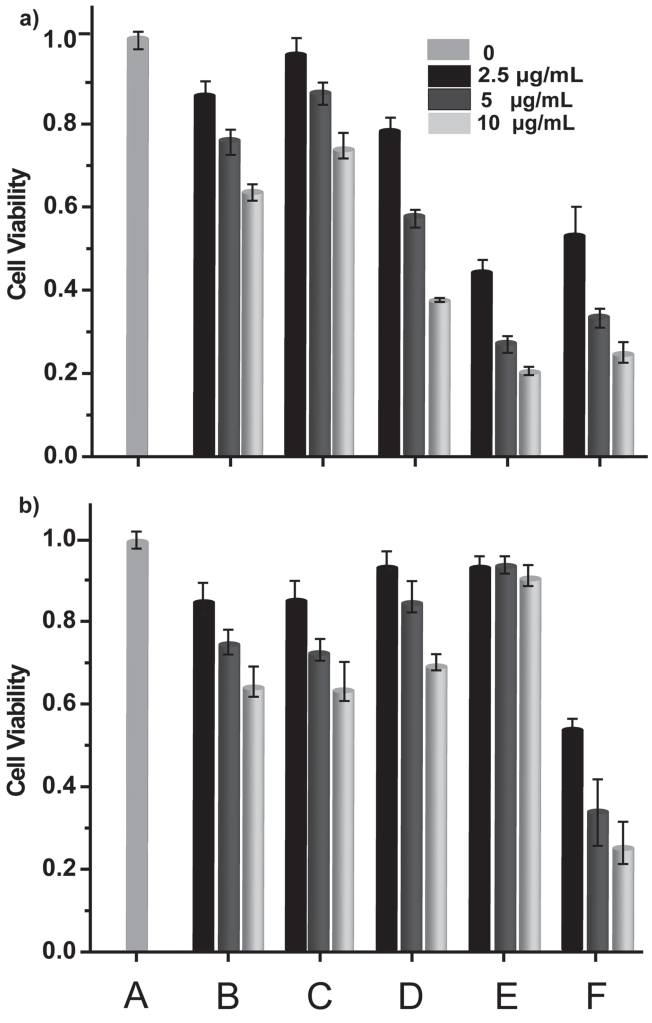

Figure 6. Cell viability MTT assay of a) HeLa cells and b) A549 cells treated with A) control, B) CPT, C) FMSN@CPT, D) FMSN@CPT-FA, E) FMSN@CPT-TAT/FA-CS-Cit, and F) FMSN@CPT-TAT (left to right), respectively. B vs E, $p < 0.001$; C vs E, $p < 0.001$; D vs E, $p < 0.001$; F vs E, $p < 0.05$.

recorded on a Micromeritics ASAP 2020M automated sorption analyzer. UV-Vis absorption spectra were recorded using a Varian Cary300 spectrophotometer equipped with a 1 cm path length quartz cell. ^1H and ^{13}C NMR spectrawere recorded on Bruker AV400 NMR spectrometer in D_2O. Fourier transform infrared (FT-IR) spectra were recorded on a BioRad Win-IR instrument using KBr method. Zeta potentials (ζ-potential) were estimated on a Zeta Potential/BI-90Plus particle size analyzer (Brookhaven, USA).

Synthesis of Fe_3O_4@$mSiO_2$ Nanoparticles (FMSN): Uniform 10 nm sized Fe_3O_4 nanocrystals were synthesized as follows: $FeCl_3{\cdot}6H_2O$ (2.43 g) and $FeCl_2{\cdot}4H_2O$ (1.195 g) were dissolved in H_2O (20 mL). The solution was stirred at 90 °C for 10 min. Then $NH_3{\cdot}H_2O$ (6 mL) and oleic acid (0.4 g) were added to the solution, followed by another 3 h of stirring. The mixture was washed with water and absolute ethanol several times. The Fe_3O_4 nanocrystals were stabilized with oleic acid and dispersed in chloroform. In a typical procedure, 15 mg of the Fe_3O_4 nanocrystals dissolved in chloroform were poured into 0.4 g of cetyltrimethylammonium bromide (CTAB) and 20 mL of water and the resulting solution was stirred vigorously for 30 min. The formation of an oil-in-water microemulsion resulted in a turbid brown solution. Then, the mixture was heated up to 60 °C and aged at that temperature for 10 min under stirring to evaporate the chloroform, resulting in a transparent black Fe_3O_4/CTAB solution. 1 mg of fluorescein isothiocyanate (FITC) was dissolved in 545 μL of absolute ethanol and mixed with 2.2 μL of aminopropyltriethoxysilane (APTES) for 2 h. 5 mL of the aqueous CTAB-stabilized Fe_3O_4 solution was added into a solution of 43 mL of distilled water and 350 μL of sodium hydroxide (2 M) and heated to 80 °C. For higher concentration of iron oxide materials, the solution may need to be heated at lower temperature (65–70 °C) in order to avoid the coalescence of the mesoporous silica in forming large clumps of materials. After the temperature had stabilized, 0.6 mL of the ethanolic FITC-APTES solution was mixed with 0.5 mL of tetraethylorthosilicate (TEOS) and added slowly into the aqueous solution containing the CTAB-stabilized Fe_3O_4. After 15 min of stirring, APTES was added and the solution was stirred for 3 h. The as-synthesized Fe_3O_4@$mSiO_2$-FITC NPs (FMSN-FITC) were washed 3× with ethanol to remove the unreacted species and dispersed in 20 mL of ethanol. The CTAB surfactants were removed from the mesopores by dispersing the as-synthesized materials in a solution of 160 mg of ammonium nitrate and 60 mL of 95% ethanol and heating the mixture at 60 °C for 15 min. The materials were then centrifuged and washed with ethanol.

The weight ratio of Fe_3O_4 to the total FMSN was calculated from:

$$w_{Fe_3O_4} = \frac{m_{Fe_3O_4}}{m_{FMSN}} \quad (1)$$

$$m_{Fe_3O_4} = m_{Fe}\frac{M_{Fe_3O_4}}{3M_{Fe}} \quad (2)$$

Where w_{Fe_3O4} means the weight ratio of Fe_3O_4 to the total FMSN; $m_{Fe_3O_4}$ and m_{FMSN} means the mass of Fe_3O_4 and Fe_3O_4@$mSiO_2$ nanoparticles; m_{Fe} is mass of Fe which is measured by inductively coupled plasma optical emission spectrometer (ICP-OES); M_{Fe} and $M_{Fe_3O_4}$ is the molar mass of Fe and Fe_3O_4, respectively.

TAT Peptide Attachment (FMSN-TAT): TAT peptide was covalently conjugated onto amine-functionalized FMSN through the –COOH group by using cross-linking reagents EDC and Sulfo-NHS. In this work, 0.2 mmol TAT was dissolved in phosphate buffered saline (PBS) solution (pH 6.0) followed by the addition of 0.2 mmol EDC and 0.5 mmol Sulfo-NHS. The mixture was then stirred at room temperature for 30 min to activate the carboxylic group of TAT peptide. Subsequently, the pH was adjusted to 8.0, and amine-functionalized FMSN solution (1 mg mL^{-1}) was added to the above solution, and the mixture was stirred for 24 h at room temperature. FMSN-TAT was collected by centrifugation to remove excess EDC, Sulfo-NHS and TAT. FMSN-TAT was dispersed in water and stored at 4 °C.

Preparation of Camptothecin (CPT) Loaded FMSN-TAT (FMSN@CPT-TAT): 4 mg of FMSN-TAT were mixed with 1 mL of CPT solution in DMSO (1 mg mL^{-1}). After stirring for 24 h under dark condition, the CPT-loaded particles were collected by centrifugation. To evaluate the CPT loading capacity, the supernatant solution was collected and the residual CPT content was measured by UV-Vis measurements at the wavelength of 364 nm.

Synthesis of Folic Acid-Chitosan (FA-CS) Conjugates: Folic acid (FA) was conjugated to the amino groups of chitosan (CS) based on a carbodiimide reaction. Briefly, FA, EDC, and NHS (molar ratio of FA: EDC: NHS = 1:1.2:1.2) were dissolved in anhydrous dimethyl sulfoxide (DMSO, 5 mL) under continuous stirring to activate the γ-COOH group of FA. Then the activated FA (0.05 mol/mol sugar residues of CS) was added dropwise into the CS solution. The resultant mixture was stirred at room temperature for about 24 h and then titrated to pH 9.0 with 0.1 M NaOH. The product was purified by dialysis (MWCO 3500) first against phosphate buffer (PBS, pH 7.4) for 3 days and then against distilled water for another 3 days. Finally, yellow dry FA-CS powder was collected after 48 h of lyophilization. All the processes were operated in the dark.

Introducing Citraconic Anhydride (Cit) to FA-CS (FA-CS-Cit): FA-CS (0.4 mg) was dissolved in 0.5 M $NaHCO_3$ buffer (pH 9.0, 25 mL). The solution was stirred at 4 °C for 30 min, and added with citraconic anhydride (1.39 g) slowly. The pH was kept at 9.0 adjusted with NaOH

(0.1 M). After stirring for 24 h, the mixture was purified dialysis (MWCO 3500) (×3 with distilled water). The final product (FA-CS-Cit) was obtained by lyophilyzation.

Synthesis of FMSN-TAT/FA-CS-Cit: CS-FA-Cit was incubated with FMSN-TAT in PBS buffer (pH 7.5) and the solution was stirred at 4 °C for 2 h to form FMSN-TAT/FA-CS-Cit complex through electrostatic interaction.

Synthesis of Folic Acid Attached FMSN (FMSN-FA): The activated FA (0.05 mol/mol sugar residues of CS) was added dropwise into the amine-functionalized FMSN solution. The resultant mixture was stirred at room temperature for about 24 h and then titrated to pH 9.0 with 0.1 M NaOH. The FMSN-FA was obtained by centrifugation.

pH-Induced Zeta Potential Change of FMSN–TAT/FA-CS-Ci: The FMSN-TAT/FA-CS-Cit solution was diluted to 0.1 mg mL^{-1} using PBS of pH 5.6 and 7.4, respectively, and then incubated at 37 °C. At designated time intervals, aliquot of FMSN-TAT/CS-FA-Cit solution was withdrawn and measured by the zetasizer (Brookhaven, USA).

Cell Culture: HeLa and A549 cells were grown at 37 °C in an atmosphere of 5% (v/v) CO_2 in air, in Dulbecco's modified Eagle's medium (DMEM) supplemented with 10% heat-inactivated FBS, 100 units mL^{-1} penicillin, 100 mg mL^{-1} streptomycin. The media was changed every three days, and the cells were digested by trypsin and resuspended in fresh complete medium before plating.

Cytotoxicity Assays: MTT assays were used to probe cellular viability. HeLa and A549 cells were seeded at a density of 5000 cells $well^{-1}$ (100 µL total volume per well) in 96-well assay plates. After 24 h incubation, the as-prepared simples, at the indicated concentrations, were added for further incubation of 48 h. To determine toxicity, 10 µL of MTT solution (BBI) was added to each well of the microtiter plate and the plate was incubated in the CO_2 incubator for an additional 4 h. Then the cells were lysed by the addition of 100 µL of DMSO. Absorbance values of formazan were determined with Bio-Rad model-680 microplate reader at 490 nm (corrected for background absorbance at 630 nm). Six replicates were done for each treatment group.

Cellular Uptake, Location, and Imaging: Cellular uptake was examined using flow cytometry and fluorescence microscopy. For observation by fluorescence microscopy, HeLa and A549 cells (1×10^5 cells) were cultured with FITC-labelled nanoparticles for 6 h in DMEM. After incubation, the cells were then washed three times with PBS and treated with LysoTracker Red for 30 min for lysosome staining. After washing three times with PBS, HeLa, and A549 cells were stained with Hoechst 33258 (10 ng mL^{-1}) for another 15 min to indicate the DNA (nucleus). Then 500 µL fixing solution (1% glutaraldehyde and 10% formaldehyde) was added to each well for 30 min and finally the imagings were captured using an Olympus BX-51 optical equipped with a CCD camera.

For flow cytometry, HeLa and A549 cells (2×10^5 cells per well) were seeded in 6-well plates in DMEM for 24 h before further manipulation. Cells were then treated with FITC-labelled nanoparticles (0.1 mg mL^{-1}) at 37 °C for 4 h, respectively. A single cell suspension was prepared consecutively by trypsinization, washing with PBS, and filtration through 35 mm nylon mesh. Thereafter, the cells were lifted using a cell stripper (Media Tech. Inc.), and analyzed using a FACS-Calibur flow cytometer (BD Biosciences) for FITC. The excitation wavelength and emission wavelength were 488 nm and 525 nm, respectively.

Cell Apoptosis Analysis by Flow Cytometry: Apoptosis analysis was conducted using the Annexin V-FITC (Annexin V) and propidiumiodide (PI) detection kit according to the manufacture's protocol. Briefly, HeLa and A549 cells (2×10^5 cells $well^{-1}$) were seeded in 6-well plates in DMEM for 24 h before further manipulation. After transfected with various blank or CPT-containing nanovectors at 10 µg mL^{-1} for predetermined periods of time, cells were collected by trypsinization and washed twice with PBS and resuspended in Annexin V binding buffer at 10^6 cells mL^{-1}. Further incubation was performed in Annexin V and PI at room temperature for 15 min in the dark, and then cells were subjected to flow cytometry analysis.

In Vitro and In Vivo Magnetic Resonance Imaging (MRI): For in vitro T_2-weighted MR imaging, dilutions of samples in PBS buffer solution containing 1% agarose with expected different concentrations as contrast agent were placed in a series of 5.0 mL Eppendorf tubes. For in vivo MRI, a tumor-bearing mouse model was established. The mouse hepatocellular carcinoma cells (H22 cells) were supplied by Xiangf bio (Shanghai, China) and were inoculated into the mammary fat pads of female Kunming mice (5×10^6 cells per mouse). Then FMSN nanoparticles dispersed in 0.9 wt% NaCl solution were administrated to mouse through tail-vein injection at a dose of 10 mg nanoparticles per kg body weight. All MR imaging scans were performed using a 1.5T clinical MRI instrument (Siemens Medical System). All animal procedures were in accordance with the guidelines of the Institutional Animal Care and Use Committee.

Statistical Analysis: All data were expressed in this article as mean result ± standard deviation (SD). Data were analyzed for statistical significance using Student's test. $p < 0.05$ was considered statistically significant, and $p < 0.001$ was considered highly significant. All figures shown in this article were obtained from three independent experiments with similar results. The statistical analysis was performed by using Origin 8.0 software.

Supporting Information

Supporting Information is available from the Wiley Online Library or from the author.

Acknowledgements

The authors acknowledgment financial support from National Basic Research Program of China (2012CB720602 and 2011CB936004) and the National Natural Science Foundation of China (21210002, 91213302, and 21072182).

Received: October 28, 2013
Received: December 19, 2013
Published online: March 4, 2014

[1] a) H. Koo, M. S. Huh, I.-C. Sun, S. H. Yuk, K. Choi, K. Kim, I. C. Kwon, *Acc. Chem. Res.* **2011**, *44*, 1018; b) J.-Z. Du, X.-J. Du, C.-Q. Mao, J. Wang, *J. Am. Chem. Soc.* **2011**, *133*, 17560.

[2] K. Ulbrich, V. r. Šubr, *Adv. Drug Delivery Rev.* **2004**, *56*, 1023.

[3] a) J.-H. Lee, K. Lee, S. H. Moon, Y. Lee, T. G. Park, J. Cheon, *Angew. Chem. Int. Ed.* **2009**, *48*, 4174; b) L. Tang, X. Yang, L. W. Dobrucki, I. Chaudhury, Q. Yin, C. Yao, S. Lezmi, W. G. Helferich, T. M. Fan, J. Cheng, *Angew. Chem. Int. Ed.* **2012**, *124*, 12893.

[4] D. Peer, J. M. Karp, S. Hong, O. C. Farokhzad, R. Margalit, R. Langer, *Nat. Nanotechnol.* **2007**, *2*, 751.

[5] a) D. Mandal, A. Nasrolahi Shirazi, K. Parang, *Angew. Chem. Int. Ed.* **2011**, *50*, 9633; b) U. Koppelhus, T. Shiraishi, V. Zachar, S. Pankratova, P. E. Nielsen, *Bioconjugate Chem.* **2008**, *19*, 1526.

[6] a) M. Duvvuri, J. P. Krise, *Front. Biosci.* **2005**, *10*, 1499; b) G. D. Wang, E. Reed, Q. Q. Li, *Oncol. Rep.* **2004**, *12*, 955.

[7] a) Z. Zhou, Y. Shen, J. Tang, M. Fan, E. A. Van Kirk, W. J. Murdoch, M. Radosz, *Adv. Funct. Mater.* **2009**, *19*, 3580; b) R. Bahadur. K. C, B. Thapa, P. Xu, *Mol. Pharm.* **2012**, *9*, 2719; c) R. Mo, Q. Sun, J. Xue, N. Li, W. Li, C. Zhang, Q. Ping, *Adv. Mater.* **2012**, *24*, 3659; d) C. Drappier, A.-L. Wirotius, K. Bathany, E. Ibarboure, O. Condassamy, E. Garanger, S. Lecommandoux, *Polym. Chem.* **2013**, *4*, 2011; e) C. Drappier, H. Oliveira, O. Sandre, E. Ibarboure, S. Combet, E. Garanger, S. Lecommandoux, *Faraday Discuss.* **2013**, *166*, 83.

[8] S. Biswas, N. S. Dodwadkar, P. P. Deshpande, V. P. Torchilin, *J. Controlled Release* **2012**, *159*, 393.

[9] L. Pan, Q. He, J. Liu, Y. Chen, M. Ma, L. Zhang, J. Shi, *J. Am. Chem. Soc.* **2012**, *134*, 5722

[10] a) E. Jin, B. Zhang, X. Sun, Z. Zhou, X. Ma, Q. Sun, J. Tang, Y. Shen, E. Van Kirk, W. J. Murdoch, M. Radosz, *J. Am. Chem. Soc.* **2012**, *135*, 933; b) D. Sarko, B. Beijer, R. G. Boy, E.-M. Nothelfer, K. Leotta, M. Eisenhut, A. Altmann, U. Haberkorn, W. Mier, *Mol. Pharm.* **2010**, *7*, 2224.

[11] J. Zhang, Z.-F. Yuan, Y. Wang, W.-H. Chen, G.-F. Luo, S.-X. Cheng, R.-X. Zhuo, X.-Z. Zhang, *J. Am. Chem. Soc.* **2013**, *135*, 5068.

[12] a) F. Scherer, M. Anton, U. Schillinger, J. Henkel, C. Bergemann, A. Kruger, B. Gansbacher, C. Plank, *Gene Ther.* **2002**, *9*, 102; b) B. P. Barnett, A. Arepally, P. V. Karmarkar, D. Qian, W. D. Gilson, P. Walczak, V. Howland, L. Lawler, C. Lauzon, M. Stuber, D. L. Kraitchman, J. W. M. Bulte, *Nat. Med.* **2007**, *13*, 986; c) L. Cheng, K. Yang, Y. Li, J. Chen, C. Wang, M. Shao, S.-T. Lee, Z. Liu, *Angew. Chem. Int. Ed.* **2011**, *50*, 7385.

[13] a) C. Chen, J. Geng, F. Pu, X. Yang, J. Ren, X. Qu, *Angew. Chem. Int. Edit.* **2011**, *50*, 882; b) E. Climent, R. Martínez-Máñez, F. Sancenón, M. D. Marcos, J. Soto, A. Maquieira, P. Amorós, *Angew. Chem. Int. Ed.* **2010**, *49*, 7281.

[14] a) Y. Lee, S. Fukushima, Y. Bae, S. Hiki, T. Ishii, K. Kataoka, *J. Am. Chem. Soc.* **2007**, *129*, 5362; b) Y. Shen, Z. Zhou, M. Sui, J. Tang, P. Xu, E. A. V. Kirk, W. J. Murdoch, M. Fan, M. Radosz, *Nanomedicine* **2010**, *5*, 1205; c) S. Guo, Y. Huang, Q. Jiang, Y. Sun, L. Deng, Z. Liang, Q. Du, J. Xing, Y. Zhao, P. C. Wang, A. Dong, X.-J. Liang, *ACS Nano* **2010**, *4*, 5505.

[15] Z.-G. Yue, W. Wei, P.-P. Lv, H. Yue, L.-Y. Wang, Z.-G. Su, G.-H. Ma, *Biomacromolecules* **2011**, *12*, 2440.

[16] L. A. Austin, B. Kang, C.-W. Yen, M. A. El-Sayed, *J. Am. Chem. Soc.* **2011**, *133*, 17594.

[17] a) J. Kim, H. S. Kim, N. Lee, T. Kim, H. Kim, T. Yu, I. C. Song, W. K. Moon, T. Hyeon, *Angew. Chem. Int. Ed.* **2008**, *120*, 8566; b) M. Liong, J. Lu, M. Kovochich, T. Xia, S. G. Ruehm, A. E. Nel, F. Tamanoi, J. I. Zink, *ACS Nano* **2008**, *2*, 889.

[18] F. M. Kievit, O. Veiseh, N. Bhattarai, C. Fang, J. W. Gunn, D. Lee, R. G. Ellenbogen, J. M. Olson, M. Zhang, *Adv. Funct. Mater.* **2009**, *19*, 2244.

[19] a) R. Xie, S. Hong, L. Feng, J. Rong, X. Chen, *J. Am. Chem. Soc.* **2012**, *134*, 9914; b) J.-M. Oh, S.-J. Choi, G.-E. Lee, S.-H. Han, J.-H. Choy, *Adv. Funct. Mater.* **2009**, *19*, 1617.

[20] a) K. Yang, L. Hu, X. Ma, S. Ye, L. Cheng, X. Shi, C. Li, Y. Li, Z. Liu, *Adv. Mater.* **2012**, *24*, 1868; b) Q. Tian, J. Hu, Y. Zhu, R. Zou, Z. Chen, S. Yang, R. Li, Q. Su, Y. Han, X. Liu, *J. Am. Chem. Soc.* **2013**, *135*, 8571.